



Solar-wind energy complementary coupling realizes magnetic-field assisted efficient photocatalytic CO₂ reduction

Biao Kong^a, Yuqi Ren^a, Maochang Liu^{b,*}, Jiancheng Zhou^{a,*}, Ke Wang^a, Nan Wang^a, Naixu Li^{a,*}

^a School of Chemistry and Chemical Engineering, Southeast University, No.2 Dongnandaxue Road, Nanjing 211189, Jiangsu, PR China

^b International Research Center for Renewable Energy, State Key Laboratory of Multiphase Flow in Power Engineering, Xi'an Jiaotong University, No.28 Xianning West Road, Xi'an 710049, Shaanxi, PR China

ARTICLE INFO

Keywords:

Photocatalysis
Muti-field coupling
TiO₂
Z-scheme
CO₂ reduction

ABSTRACT

We report the synthesis of a Z-scheme monolithic photocatalyst in the form of copper foam (CF) supported TiO₂ combining Cu₂O and Ag nanoparticles (CF@TiO₂/Cu₂O-Ag). The designed catalysts with efficient charge separation show superior photocatalytic activity toward CO₂ reduction, with a maximum CO yielding rate of 25.58 μmol·g⁻¹·h⁻¹. More importantly, we develop a solar-wind energy complementary device, which enables the strong coupling of the magnetic field into the photocatalytic reaction. Specifically, the in-situ space electric field generated from the wind-driven induced electromotive force further enhances the separation and transportation of photogenerated charge carriers in the Z-scheme system. The productivity of CO in the proof-of-concept device based on the use of CF@TiO₂/Cu₂O-Ag catalyst reaches 71.66 μmol·g⁻¹·h⁻¹. This study provides an ideal approach for reinforcing photocatalytic CO₂ reduction through muti-field coupling and highlights the prospect of solar-wind energy coupled photocatalysis.

1. Introduction

The continuous consumption of fossil energy leads to excessive emissions of CO₂[1]. The technology of capturing and storing carbon dioxide served as an efficacious method of reducing CO₂ emissions[2]. Compared with CO₂ capture and separation technologies, the photocatalytic conversion of CO₂ which uses H₂O as raw materials has drawn people's attention in recent years due to its green and economic merits, solar energy is inexhaustible and harmless to the environment[3,4]. Various photocatalysts such as TiO₂, ZnO, and CeO₂ have been applied in CO₂ reduction[5–7]. TiO₂ is one of the most popular photocatalysts and is being investigated widely, attributed to its outstanding photostability, nontoxicity, environmental friendliness, and low cost[8,9]. However, TiO₂ still has some drawbacks such as fast recombination of photogenerated charges and relatively wide band gap, which resulted in low quantum efficiency and the limited utilization rate of visible light, respectively[10,11].

The construction of heterojunction is widely considered a practical method to improve charge separation efficiency and enhance photocatalytic activity[12–14]. The Z-scheme system is a kind of

heterojunction system named in which the transportation pathway of charge carriers consists of a two-step photoexcitation process that is similar to the English letter “Z”[15,16]. The component photocatalysts' highly reducing and oxidizing ability can be maintained in the Z-scheme system, which is different from the traditional type-II heterojunction[17, 18]. The cuprous oxide (Cu₂O) has a narrow band gap (ranging from 2.0 to 2.2 eV) and can utilize visible light more effectively. Besides, the potential of favoring CO₂ activation and abundant reserves make Cu₂O one of the most attractive CO₂ photoreduction semiconductor materials [19,20]. However, the photostability of Cu₂O is scarce[21]. So, a proper co-catalyst that can enhance the stability of Cu₂O is necessary. Generally, noble metals including Ag, Au, and Pt can act as electron-trapping agents, which promotes photocatalytic activity[22,23].

Within almost fifty years of development, the technology in the photocatalytic field has developed into a relatively complete and mature system[24,25]. Yang et al. improved the CH₄ productivity of ZnIn₂S₄/TiO₂ by constructing a Z-scheme system, which is 38 times higher than undecorated ZnIn₂S₄[5]. Xiong et al. synthesized Pt and Cu₂O co-decorated TiO₂ nanocrystals, boosting the TiO₂ photocatalytic activity and realizing a high selectivity of CO₂ to CH₄ conversion(96.6%)

* Corresponding authors at: School of Chemistry and Chemical Engineering, Southeast University, No.2 Dongnandaxue Road, Nanjing 211189, Jiangsu, PR China.
E-mail addresses: maochangliu@mail.xjtu.edu.cn (M. Liu), jczhou@seu.edu.cn (J. Zhou), naixuli@seu.edu.cn (N. Li).

[9]. However, the capability of the photocatalysts to generate and transfer the photo-induced charge carriers is limited by their intrinsic properties[26]. In recent years, the coupling of external fields in photocatalysis draw people's attention[27,28]. Introducing external fields into the photocatalytic reaction process such as photo-thermal, photo-electric, and photo-magnetic coupling is a feasible and manageable method to promote photocatalytic activity[29–31]. For example, in photo electrocatalysis, with the application of the external bias, a better separation of photogenerated charges can be promoted[32]. Many researchers have tried to realize the photo-magnetic field coupling in photocatalysis[33–35]. It has been reported that the Lorentz force generated by a magnetic field is able to make the photo-induced carriers deviate and achieve the purpose of separation and transfer, leading to better photocatalytic activity[36,37]. Gao et al. investigated the photocatalytic performance of TiO_2 nanobelts under photo-magnetic field coupling conditions. The Lorentz forces induced by the magnetic field affected the moving directions of photogenerated electrons and holes. Separating them in contrary directions, thus inhibit the charge recombination in TiO_2 bulk and provide more opportunities for carriers to participate in the photocatalytic reaction[37]. Besides, they also

successfully optimized the separation of the carriers in CdS and improved the H_2 production of Au/CdS to 110% through in situ micro electric field generated by induced electromotive force through a rotating magnetic field according to the Faraday law of electromagnetic induction[38]. Meanwhile, applying an external field in photocatalysis often comes with more consumption of energy.

Herein, we constructed monolithic Z-scheme $\text{CF@TiO}_2/\text{Cu}_2\text{O}-\text{Ag}$ photocatalysts on the copper foam substrate (CF) to promote the separation of carriers and boost the CO_2 conversion efficiency. We also designed a solar-wind photocatalytic reactor, in which there is a rotating magnetic field device with two opposite neodymium magnetic shoes driven by clean energy–wind. Successfully enhanced the photocatalytic efficiency of the metal/Z-scheme system. The charge separation of catalysts that grows on the metallic substrate will be enhanced due to the in-situ spacial electric field resulting from the induced electromotive force generated from the metallic substrate cutting magnetic induction lines. This strategy extends the application of external field, especially for introducing a magnetic field in the improvement of photocatalytic activity, and also provides an idea of photocatalysis with renewable energy.

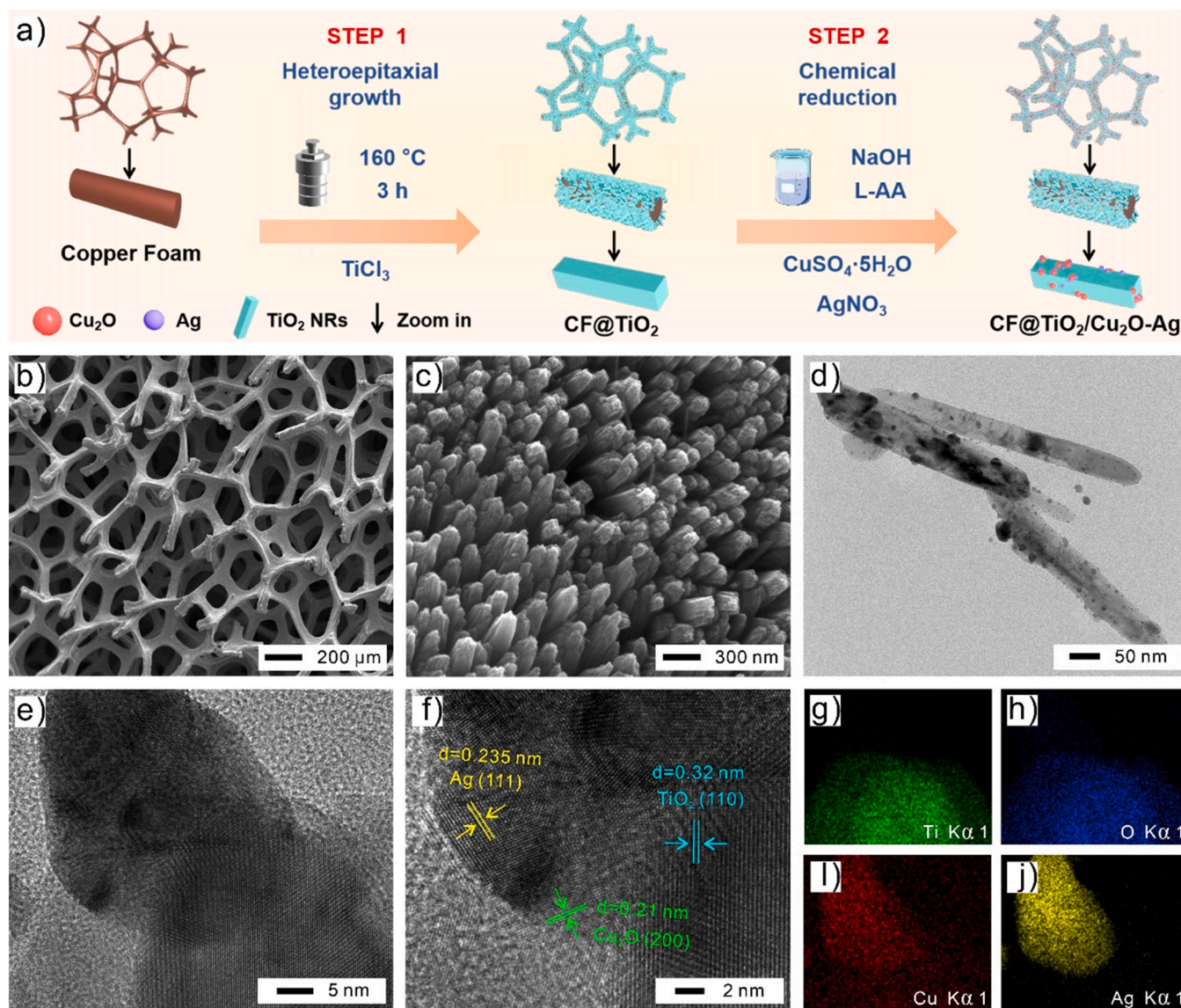


Fig. 1. (a) The fabrication process of the monolithic $\text{CF@TiO}_2/\text{Cu}_2\text{O}-\text{Ag}$ catalysts, (b-c) The SEM images of copper foam and TiO_2 nanorods grown on the copper foam, (d) TEM images of the $\text{TiO}_2/\text{Cu}_2\text{O}-\text{Ag}$ catalysts, (e-f) HR-TEM images of the $\text{TiO}_2/\text{Cu}_2\text{O}-\text{Ag}$ catalysts, (g-j) The EDS images of Ti, O, Cu and Ag distribution of the $\text{TiO}_2/\text{Cu}_2\text{O}-\text{Ag}$ catalysts.

2. Results and discussion

As is illustrated apparently in Fig. 1a, the CF@TiO₂/Cu₂O-Ag monolithic photocatalysts can be manufactured through two steps. Firstly, monolithic CF@TiO₂ nanorod arrays can be prepared with the heteroepitaxial growth method[39,40]. In this process, the copper foam (CF) just serves as a support that supplies growing space for TiO₂ nanorod arrays. Therefore, the quality of the rutile TiO₂ nanorods can be weighted by comparing the mass difference of the drying sample before and after the solvothermal reaction, the relevant data are added as Table S2 in the SI. Secondly, Cu₂O and Ag NPs were deposited onto TiO₂ NRs through a polished chemical reduction method[41]. The reducing agent was L-ascorbic acid (L-AA)[42,43]. The depositing amount of Cu₂O and Ag NPs can be regulated by controlling the dosage of the CuSO₄ and AgNO₃ added in the precursor solution.

The morphological features and microstructure of the photocatalysts were synthesized were investigated in detail by SEM and TEM. Fig. 1b reveals the 3D nanonetwork of the copper foam clearly, CF has a criss-cross reticular structure and smooth surface which supply a suitable growing condition for TiO₂ NRs. As is shown in Fig. 1c, a highly uniform and densely packed array of nanorods cladding on the surface of the skeleton of the CF, the rutile TiO₂ features tetragonal rods with a length of 800–1000 nm and a diameter of 100 nm. Due to the low contents and tiny size of Cu₂O and Ag NPs, more details of CF@TiO₂/Cu₂O-Ag catalysts are obtained from high-resolution TEM (Fig. 1d–j). Many irregular small Cu₂O and Ag particles with an average size of 15 nm are observed on the surfaces of the TiO₂ NRs for CF@TiO₂/Cu₂O-Ag (Fig. 1d–e). Fig. 1f shows the crystalline lattice characteristic of the CF@TiO₂/Cu₂O-Ag sample. The lattice fringe spacings of 0.21 nm and 0.235 nm can be matched to the (200) plane of Cu₂O and (111) plane of Ag respectively while the measured distances of 0.32 nm are attributed to the (110) plane of rutile TiO₂[44–46]. The EDS mappings shown in Fig. 1g–j reveal the spatial distribution and existence of elemental Ti, O, Cu and Ag distinctly. Furthermore, the element of Ag is loaded on the position where the element Cu is plentiful. According to the analysis mentioned above, rutile TiO₂ nanorod arrays were grown on the CF substrate and decorated with Cu₂O and Ag nanoparticles successfully.

X-ray diffraction (XRD) was used to examine the crystal structure of the various TiO₂-based samples we prepared. As Fig S1 reveals, three sharp characteristic peaks at $2\theta = 43.3^\circ$, 50.4° , and 74.1° are the (111), (200), and (220) diffraction planes of pure metallic copper (JCPDS No.04–0836)[47]. Other diffraction peaks at $2\theta = 27.4^\circ$, 36.1° , 41.2° , 54.3° , 56.6° , and 69.7° can be attributed to tetragonal rutile TiO₂ (JCPDS No.21–1276)[48]. However, no typical peaks of Cu₂O and Ag nanoparticles were observed in these XRD patterns because of the low deposition content. The UV-Vis diffuse reflectance spectra test showed the optical response of TiO₂, TiO₂/0.6Cu₂O, and TiO₂/0.6Cu₂O-0.6Ag catalysts (Fig S2). The pure rutile TiO₂ showed a wide band gap and the absorption edge is about 410 nm, this indicates that rutile TiO₂ can only absorb UV light effectively[49,50]. After loading Cu₂O, the absorption edge presented a slight shift and the light absorption in visible light increased[51]. With the deposition of Ag, the visible light absorption intensity further increased and a new absorption peak range from 400 to 600 nm appeared, which can be attributed to the surface plasmon resonance effect of Ag nanoparticles[52]. We applied X-ray photoelectron spectroscopy (XPS) to research the chemical compositions and valence states of the elements in prepared catalysts. Fig S3a shows the full spectra of TiO₂/0.6Cu₂O-0.6Ag catalysts. The peaks in Fig S3c are from O 1s spectra, the peak of the lattice oxygen in Cu₂O and TiO₂ is located at 529.75 eV, while the peak at 530.91 eV can be ascribed to the chemically adsorbed oxygen[53,54]. Fig S3d displays the spectrum of Ti 2p, there are two peaks at 458.56 (Ti (IV) 2p_{3/2}) and 464.29 eV (Ti (IV) 2p_{1/2})[53]. Two XPS peaks at a binding energy of 932.26 eV and 951.96 eV which are shown in Fig S3e can be ascribed to Cu 2p_{3/2} and Cu 2p_{1/2}, respectively[55,56]. There are no Cu 2p satellite peak appears in the region of 935 to 945 eV, which confirms the existence of Cu₂O[56,

57]. Additionally, the LMM Auger electron energy spectrum of Cu of pure Cu₂O, TiO₂/0.6Cu₂O, and TiO₂/0.6Cu₂O-0.6Ag is also given in Fig S4. The strong peak at Kinetic energy = 916.3 eV further confirms that most Cu atoms are present in the form of Cu₂O in the catalysts we prepared, no apparent peak of Cu⁰ (Kinetic energy is about 918.6 eV) detected in the spectrum[58,59]. The Ag 3d spectra (Fig S3f) shows two main peaks at a binding energy of 367.58 and 373.59 eV, which can be attributed to metallic Ag, peaks at 368.54 and 374.51 eV are ascribed to Ag 3d_{3/2} and Ag 3d_{5/2} of Ag⁺[41,60]. Considering the clear lattice fringes of Ag, the peaks of Ag⁺ might result from the Ag₂O formed by slight oxidation of Ag[61].

To estimate the photocatalytic activities of different catalysts, various samples are involved in the photocatalytic CO₂ reduction reaction under the same condition. In all experiments, the main products that were detected were CO and CH₄. As is shown in Fig S5, the bare copper foam (CF) substrate has little photocatalytic activity. Due to the wide band gap of rutile TiO₂, the yields of CO and CH₄ of CF@TiO₂ are only 1.24 $\mu\text{mol}\cdot\text{g}^{-1}$ and 0.25 $\mu\text{mol}\cdot\text{g}^{-1}$. After introducing co-catalyst Cu₂O and balancing the loading amount (the best atomic ratio percentage of Cu to Ti is 0.6%), the productivity of CO under UV–vis light for 1 h increased sharply to 13.63 $\mu\text{mol}\cdot\text{g}^{-1}$ and the yield of CH₄ was 1.81 $\mu\text{mol}\cdot\text{g}^{-1}$ (Fig S6a). This is almost 11 times more than pure TiO₂ in CO production. Unfortunately, as with many other semiconductors that have good performance in the visible region, the photostability of Cu₂O is rare, so we introduced Ag to retard the photo corrosion of Cu₂O. Fig S6b shows the product evolution of ternary CF@TiO₂/Cu₂O-Ag catalysts. By setting the Ag/Ti molar ratio at 0.6%, the ternary CF@T/0.6Cu₂O-0.6Ag catalysts showed higher photocatalytic activities than binary CF@T/0.6Cu₂O, which yield of CO and CH₄ were 25.58 $\mu\text{mol}\cdot\text{g}^{-1}$ and 3.54 $\mu\text{mol}\cdot\text{g}^{-1}$, respectively. The photocatalytic performance of CF@TiO₂, CF@T/0.6Cu₂O, and CF@T/0.6Cu₂O-0.6Ag is displayed in Fig. 2a and the ICP-OES/MS data of as-prepared TiO₂/0.6Cu₂O-0.6Ag catalysts is listed in Table S3. After five cycles (2 h a cycle) of stability test, CF@T/0.6Cu₂O-0.6Ag catalysts showed good stability, and no obvious deactivation was detected (Fig. 2b). The slight decrease in the photocatalytic activity of CF@T/0.6Cu₂O-0.6Ag catalysts could be attributed to the Cu that generates from the photocorrosion of Cu₂O nanoparticles (Fig S7a)[59]. To further trace the carbon source of the products, we carried out the GC-MS analysis of the products generated from the ¹³CO₂ isotope experiments (Fig. 2c). The results confirm that the carbon source of the products comes from the reactant (CO₂) rather than an external carbon source. The main signal at $m/z = 29$ is assigned to ¹³CO and $m/z = 17$ can be attributed to ¹³CH₄.

To exclude that the enhanced photocatalytic CO₂ reduction performance of TiO₂/0.6Cu₂O and TiO₂/0.6Cu₂O-0.6Ag catalysts were resulted from the surface area effect, the nitrogen adsorption-desorption isotherm and corresponding Barret-Joyner-Halenda (BJH) pore size distribution were measured (Fig S8). As shown in the Fig S8a, all the samples exhibit similar isotherms of type IV curve with H3 hysteresis loop, indicating that the samples are mesoporous materials. As is listed in Table S4, The TiO₂, TiO₂/0.6Cu₂O and TiO₂/0.6Cu₂O-0.6Ag catalysts have similar BET specific surface area. With the loading of Cu₂O and Ag nanoparticles on TiO₂, the specific surface area of the catalysts decrease. The lower surface area may be due to the mesopores occupied by the Cu₂O and Ag nanoparticles. The BET specific surface area of the three kinds of catalysts prepared shows little difference, however, their activities in photocatalytic CO₂ reduction are quite different, indicating that the improved photocatalytic performance of CF@TiO₂/Cu₂O-Ag series catalysts is indeed caused by the deposition of Cu₂O and Ag nanoparticles instead of the surface area effect[62,63].

Moreover, the PL spectra can be used to research the trapping, immigration, transportation, and separation efficiency of the photo-induced carriers. Fig. 2d displays the PL spectra of each photocatalyst, two main emission peaks at 438 nm and 466 nm are attributed to rutile TiO₂ and band edge free excitons, respectively[64,65]. Pure TiO₂ showed the highest emission peak, with the loading of Cu₂O, the

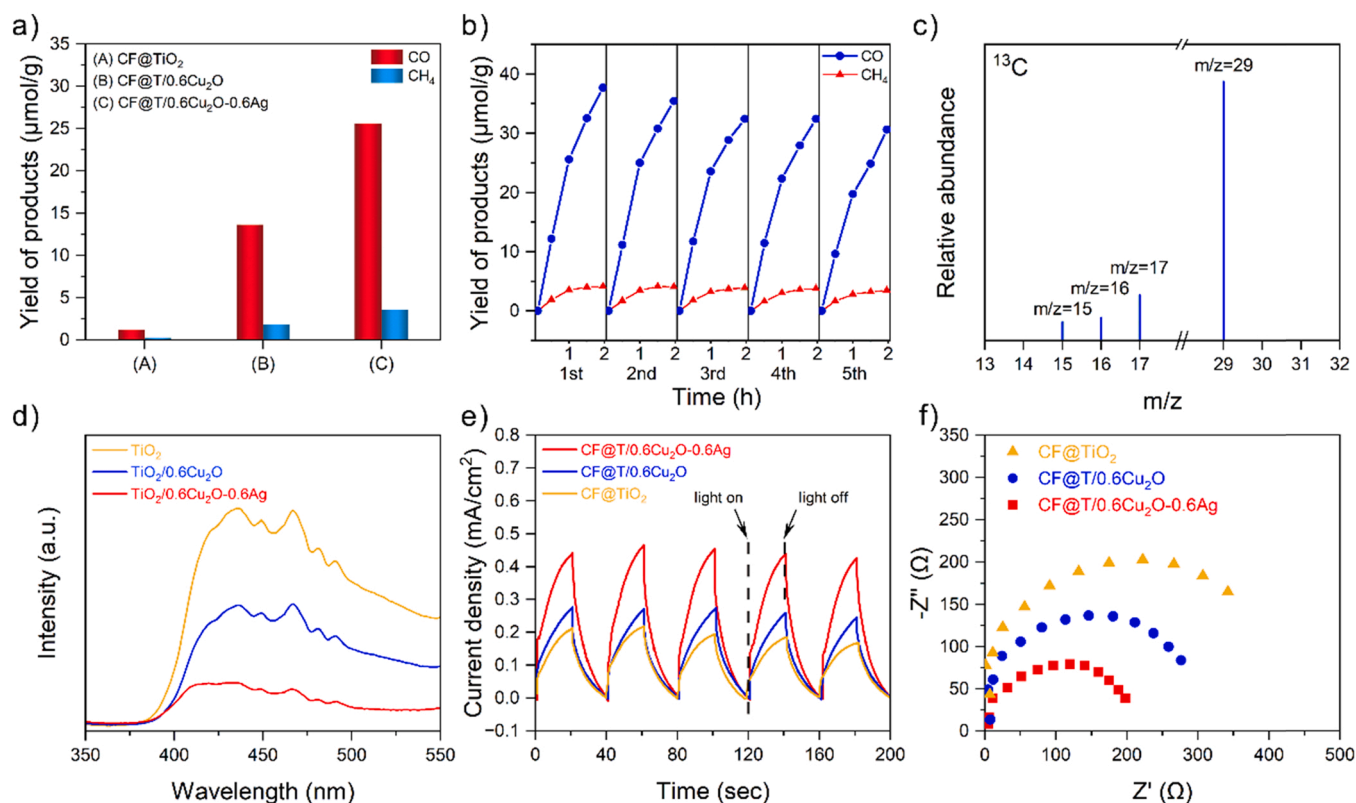


Fig. 2. (a) Yield of products of different catalysts, (b) The recycling photocatalytic production test of CF@T/0.6Cu₂O-0.6Ag catalysts, (c) GC-MS analysis of the products generated from the ¹³C₂O₂ isotope experiments of CF@T/0.6Cu₂O-0.6Ag, (d) Photoluminescence spectra of TiO₂, TiO₂/0.6Cu₂O, and TiO₂/0.6Cu₂O-0.6Ag catalysts, (e) Transient photocurrent curves of CF@TiO₂, CF@T/0.6Cu₂O, and CF@T/0.6Cu₂O-0.6Ag catalysts, (f) Electrochemical impedance spectroscopy (EIS) Nyquist plots of CF@TiO₂, CF@T/0.6Cu₂O, CF@T/0.6Cu₂O-0.6Ag catalysts.

intensity of the emission peak decreased, this is because of the heterostructures between TiO₂ and Cu₂O. Heterojunction results in an efficient charge transfer pathway, which can inhibit the recombination of photogenerated carriers. With the co-decoration of Cu₂O and Ag, the PL emission intensity was further decreased, this will be attributed to that Ag can trap the photogenerated electrons and delay their recombination with holes. The result demonstrates that the co-deposition of Cu₂O and Ag prolongs the lifetime of the charge carriers and enhances photocatalytic activities greatly. We further conducted a series of photoelectrochemical tests to verify the charge separation ability of the prepared samples. Fig. 2e shows the transient photocurrent responses of CF@TiO₂, CF@T/0.6Cu₂O, and CF@T/0.6Cu₂O-0.6Ag catalysts with five on-and-off switch cycles. Generally, more effective separation and transportation of the photo-induced carriers can be reflected by a higher photocurrent density. The density of the photocurrent increased from 0.2 mA/cm² to 0.27 mA/cm² and 0.44 mA/cm² with the loading of Cu₂O or Cu₂O and Ag, respectively. This indicates that the combined synergy of Cu₂O and Ag which Ag further captures the electrons from Cu₂O is more efficient for charge separation and transportation [66]. We also estimated the charge transfer resistance between interfaces and separation efficiency between the work electrode and electrolyte through electrochemical impedance spectroscopy (EIS) (Fig. 2f). Compared with other samples, CF@T/0.6Cu₂O-0.6Ag catalysts had the smallest semicircle, which suggests that the charge transfer resistance between the catalysts and electrolyte is the lowest and the charge transferring process is accelerated [67].

To further figure out the charge transfer pathway between TiO₂ and Cu₂O interface, we investigate the energy band structure of TiO₂ and Cu₂O. The band gap (E_g) of TiO₂ and Cu₂O was calculated by the Kubelka-Munk equation. The band gap of TiO₂ and Cu₂O were shown in Fig S9, which is 3.03 eV and 2.02 eV, respectively [68,69]. Furthermore,

the XPS valence band potentials of TiO₂ and Cu₂O were presented in Fig S10. By using the formula: $E_{VB,NHE} = \phi + E_{VB,XPS} - 4.44$, Where ϕ is the work function of the XPS instrument (4.2 eV) [70]. The maximum of the valence band (VBM) of TiO₂ is estimated to be 2.53 eV (vs. NHE) and the maximum of the valence band of Cu₂O is estimated to be 0.56 eV (vs. NHE) similarly [70,71]. So, the conduct band minimum (CBM) can be calculated with the equation: $CBM = VBM - E_g$, the CBM of TiO₂ and Cu₂O are deduced to be -0.5 eV (vs. NHE) and -1.46 eV (vs. NHE), respectively [72]. There are two possible charge transfer processes between TiO₂ and Cu₂O according to the band edge positions of TiO₂ and Cu₂O: a. conventional Type-II and b. direct Z-scheme type. Therefore, we investigated the charge transfer mechanism of the binary TiO₂/0.6Cu₂O and ternary TiO₂/0.6Cu₂O-0.6Ag catalysts through the electron paramagnetic resonance (EPR) method under simulated light irradiation. DMPO is used as spin alternation trapping reagent [73]. Fig. 3a shows the DMPO-O₂ signal of TiO₂, Cu₂O, TiO₂/0.6Cu₂O, and TiO₂/0.6Cu₂O-0.6Ag. Under dark conditions, no signal was detected. After 10 min Xe lamp irradiation, the signal intensity in the following sequence: TiO₂ < Cu₂O < TiO₂/0.6Cu₂O < TiO₂/0.6Cu₂O-0.6Ag. This may be because the conduct band potential of Cu₂O is much more negative than that of O₂/O₂⁻ (-0.33 eV vs. NHE) and photo-induced electrons in the CB of TiO₂ transferred to the VB of Cu₂O, thus inhibiting the electrons and holes in Cu₂O from recombining [74]. Fig. 3b displays the signal of DMPO-OH. Similar to Fig. 3a, there was no signal in dark conditions, and the signal intensity with irradiation in the sequence of TiO₂ < TiO₂/0.6Cu₂O < TiO₂/0.6Cu₂O-0.6Ag. Notably, no DMPO-OH signal was found in pure Cu₂O under Xe lamp irradiation for 10 min, this can be attributed to the potential of OH⁻/OH (2.40 eV vs. NHE) being more positive than the valence band potential of Cu₂O so that the photo-induced holes in the valence band of Cu₂O unable to oxidize OH⁻ to ·OH [75]. In Fig S11a, we can observe the characteristic

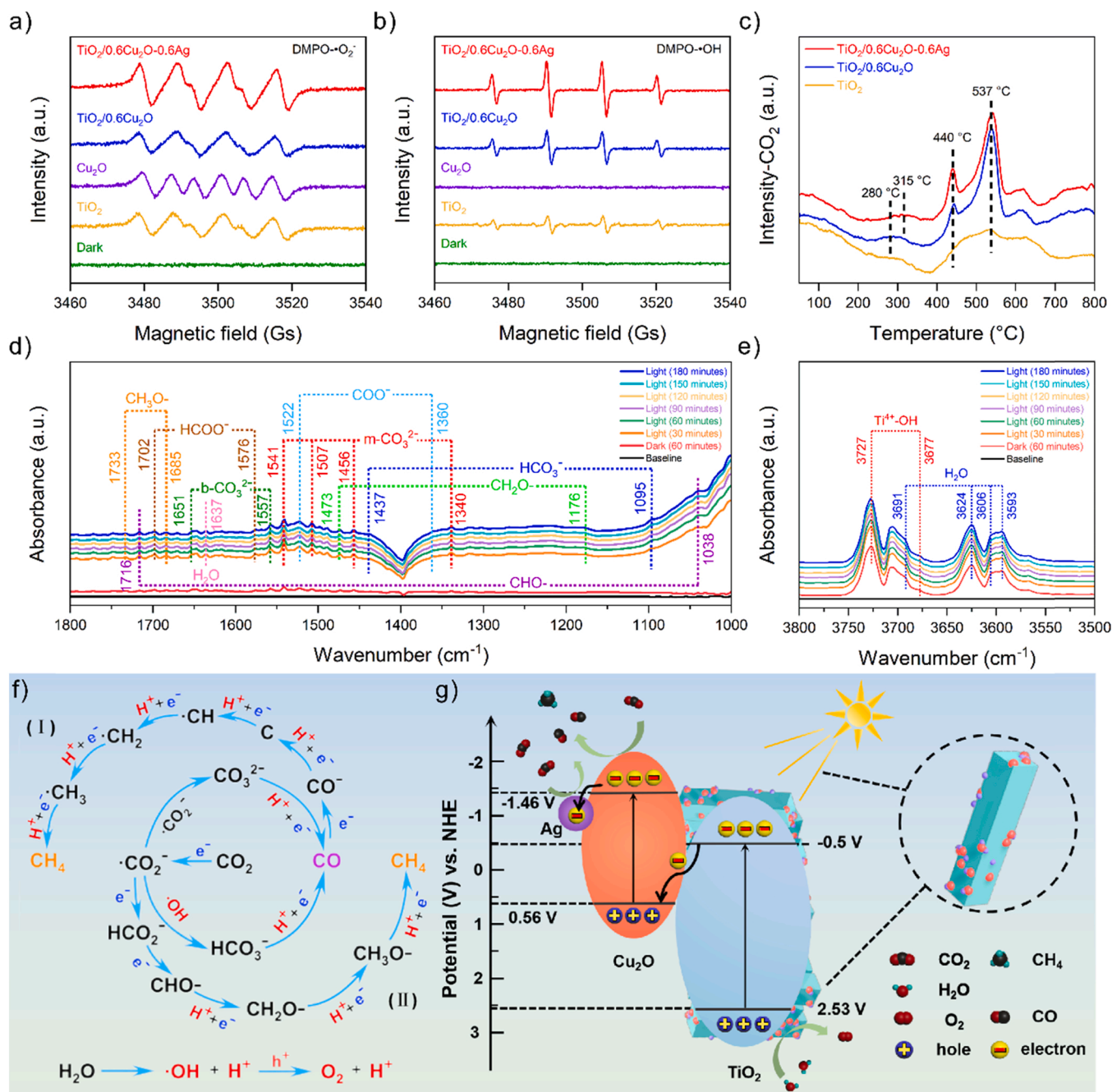


Fig. 3. (a-b) EPR spectra of DMPO-O₂ and DMPO-OH radical active species with Xe lamp irradiation for 10 min over different catalysts, (c) CO₂-TPD spectra of TiO₂, TiO₂/0.6Cu₂O, TiO₂/0.6Cu₂O-0.6Ag catalysts, (d-e) In-situ DRIFTS spectra of TiO₂/0.6Cu₂O-0.6Ag catalysts under CO₂/H₂O condition, (f) Possible reaction pathways in the photoreduction of CO₂ to CO and CH₄, (g) Proposed reaction mechanism for TiO₂/0.6Cu₂O-0.6Ag catalyst in photocatalytic CO₂ reduction reaction under UV-Vis light irradiation.

peaks of Cu 2p shift slightly toward higher binding energy after contacting with TiO₂, reaffirming the electrons transfer from Cu₂O to TiO₂, which agree with the opposite binding energy shift of Ti (Fig S11b). Such shifts of binding energy prove an intimate contact between TiO₂ and Cu₂O at their interfaces. The TiO₂ has lower Fermi level than Cu₂O, as the TiO₂ composited with Cu₂O, electrons will transfer from Cu₂O to TiO₂ to regain the balance of Fermi level, an internal electric field at the interface which pointing from Cu₂O to TiO₂ is generated, this is consistent with the XPS analysis[72,76]. In consideration of the analysis of EPR and XPS, the more reasonable mode to explain the charge transfer process of TiO₂/Cu₂O composite catalysts is the direct Z-scheme system.

CO₂ temperature-programmed desorption was used to investigate the absorption and interaction between prepared catalysts and CO₂ molecules. There are various absorption modes of CO₂, the peak ranged from 75 °C to 180 °C correspond to the decomposition of molecularly adsorbed CO₂, while peaks from 180–380 °C, 380–550 °C, 550–650 °C belongs to HCO₃⁻, b-CO₃²⁻ and m-CO₃²⁻, respectively[77,78]. As Fig. 3c illustrates, there are no apparent desorption peaks of TiO₂ for CO₂ absorption, proving the poor interaction between CO₂ and TiO₂. After loading Cu₂O, two obvious CO₂ desorption peaks are observed, which are located at 440 °C and 537 °C, this can be attributed to the bonding of the C atom in CO₂ with the Cu site which enhances the CO₂ absorption efficiency[79,80]. When Ag is further deposited on TiO₂/Cu₂O catalysts.

The peak intensity at 440 °C and 537 °C increased and the desorption peak of TiO₂/0.6Cu₂O at 280 °C shifted to a higher temperature of 315 °C[81]. All this evidence indicates that the introduction of Cu₂O and Ag nanoparticles can enhance the chemisorption of CO₂ and then improve photocatalytic efficiency.

Fig. 3d-e show the in situ DRIFTS spectra of the TiO₂/0.6Cu₂O-0.6Ag catalysts during the photocatalytic CO₂ reduction reaction which aimed to detect the key intermediates and reveal the possible conversion pathways of CO₂ during the photocatalytic process. After nitrogen purging for 60 min, the reaction system was purged with a mixture gas of CO₂ and H₂O. The samples are irradiated by simulated light and the peaks were recorded every 30 min. Fig. 3d depicts the spectra from 1800 cm⁻¹ to 1000 cm⁻¹, there were four different recorded adsorption modes for surface-adsorbed CO₂. That is, m-CO₃²⁻ (1340, 1456, 1507 and 1541 cm⁻¹), b-CO₃²⁻ (1557 and 1651 cm⁻¹), HCO₃⁻ (1095 and 1437 cm⁻¹) and COO⁻ (1360 and 1522 cm⁻¹) [82–87]. Particularly, peaks belonging to HCOO⁻ (1576 and 1702 cm⁻¹) were detected and it is an important intermediate for the photocatalytic reduction of CO₂ to CO [84]. In addition, some other intermediates such as CHO⁻ (1038 and 1716 cm⁻¹), CH₂O⁻ (1176 and 1473 cm⁻¹), and CH₃O⁻ (1685 and 1733 cm⁻¹) were also found, proving the feasibility of CO₂ to CH₄ conversion [85–87]. The adsorption band ranged from 3800 to 3500 cm⁻¹ (Fig. 3e) are assigned to the stretching vibration of H-bound OH groups and H₂O in the form of physical adsorption (3593, 3606, 3624, and 3691 cm⁻¹). Meanwhile, the peaks at 3677 and 3727 cm⁻¹ can be attributed to Ti⁴⁺-OH and confirmed the bonding of TiO₂ and H₂O [88].

Based on the results and discussions mentioned above, we propose the possible CO₂ conversion process (Fig. 3f) and mechanism of TiO₂/0.6Cu₂O-0.6Ag in photocatalytic reaction (Fig. 3g). Fig. 3f displays the adsorbed CO₂ molecules obtain electrons to form COO⁻, COO⁻ further obtain electrons and protons to generate HCO₃⁻ or HCOO⁻. HCO₃⁻ or HCOO⁻ can further generate CO and release from the adsorption sites or continue to gain electrons and protons to the form of CH₄ through the carbene (I) or formaldehyde (II) pathway [83,84,89]. As shown in Fig. 3g, after the solar irradiation, the TiO₂ and Cu₂O are photoexcited thus generating electrons and holes. Attribute to the intimate interfacial contact between TiO₂ and Cu₂O, the electrons in the CB of TiO₂ can transfer to the VB of Cu₂O fluently and recombine with the holes, which follow the Z-scheme charge transfer pathway [90]. The holes in the VB of TiO₂ will oxidize the H₂O to O₂ and protons while the electrons in the CB of Cu₂O were used for the reduction of CO₂ to generate CO and CH₄ [72, 90]. Besides, the Ag nanoparticles can act as a reservoir to capture the enriched electrons to generate CH₄ and retard the photo corrosion of Cu₂O [42,55].

The unsatisfied conversion efficiency of solar energy inhibits the practical application of photocatalysis. To improve the photocatalytic activity of semiconductors, many researchers coupled the photocatalytic process with an external field to introduce extra energy to the system [27,28] Gao et al. applied the micro-electric potential in metals through a magnetic field [38]. There will be Lorentz force inside the metal when the metallic conductor is cutting the magnetic induction lines, thus the charges inside the metal will be affected and polarize spontaneously

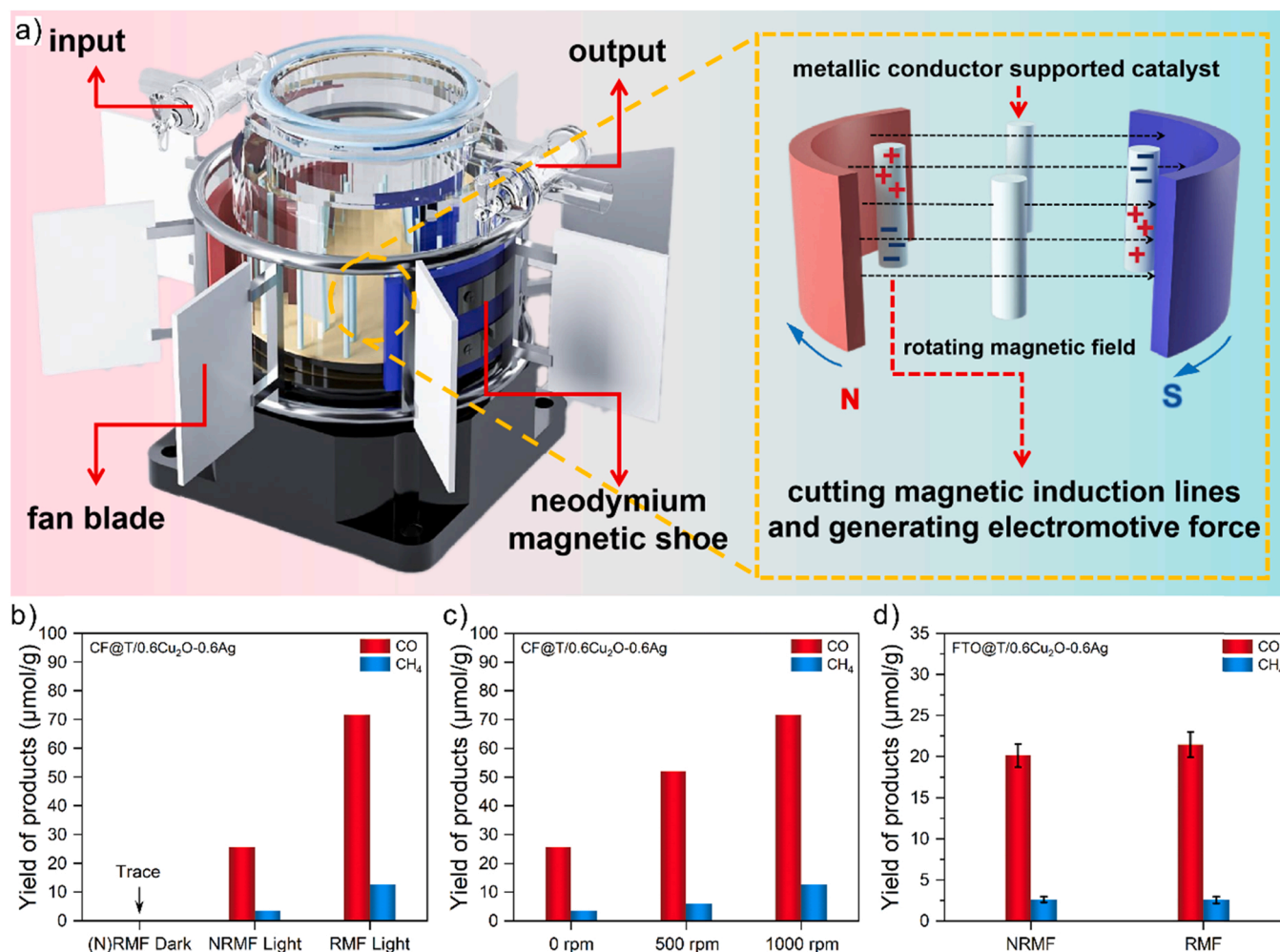


Fig. 4. (a) Diagram of solar-wind photocatalytic reactor, (b) Yield of products of CF@TiO₂/0.6Cu₂O-0.6Ag catalysts under different conditions, (c) Yield of products of CF@TiO₂/0.6Cu₂O-0.6Ag catalysts under RMF with different rotating speed, (d) Yield of products of FTO@TiO₂/0.6Cu₂O-0.6Ag catalysts under RMF and NRMF conditions.

according to the direction of Lorentz force. When coating the photocatalysts on its surface, the space electric field could affect the photo-induced carriers to deviate contrarily and thus achieve higher photocatalytic efficiency.

Considering the analysis above, we designed a solar-wind photocatalytic reactor (Fig. 4a). This reactor is composed of the photocatalytic reactor, a rotating magnetic device with two opposite neodymium magnetic shoes driven by wind. We put the CF@T/0.6Cu₂O-0.6Ag catalysts into the rotating magnetic field (RMF), the CF@T/0.6Cu₂O-0.6Ag catalysts are vertical to the magnetic induction line, so when the magnetic field rotating, the CF strips will cut the magnetic induction line and generating alternating-direction motional electromotive force. Fig S12 shows the solar-wind photocatalytic system in the experimental condition. In the experimental condition, we use electricity to power the system and a Xe lamp to simulate the sunlight. We also simulate the different wind velocities by adjusting the rotating speed of the magnetic

tile from 0 to 1000 rpm, the demonstration video is attached in SI.

Supplementary material related to this article can be found online at [doi:10.1016/j.apcatb.2023.122858](https://doi.org/10.1016/j.apcatb.2023.122858).

Fig. 4b displays the products that CF@T/0.6Cu₂O-0.6Ag catalysts yield under different circumstances within one hour. There are no products detected in the dark whether the RMF (Rotating Magnetic Field) is applied or not because no catalysts are activated to generate electrons and holes that participate in the CO₂ reduction reaction. The productivity of CO and CH₄ increased sharply from 25.58 $\mu\text{mol}\cdot\text{g}^{-1}$ and 3.54 $\mu\text{mol}\cdot\text{g}^{-1}$ in normal conditions to 71.66 $\mu\text{mol}\cdot\text{g}^{-1}$ and 12.59 $\mu\text{mol}\cdot\text{g}^{-1}$ with the introduction of 1000 rpm RMF under Xe lamp irradiation, respectively. It was almost three times. Fig. 4c depicts the comparison of the productivity of CF@T/0.6Cu₂O-0.6Ag under different rotating speeds. The productivity gained along with the boost of rotating speed. This is because the motional electromotive force is related to the relative movement speed. As is shown in Fig. 4d, when grow the TiO₂/0.6Cu₂O-

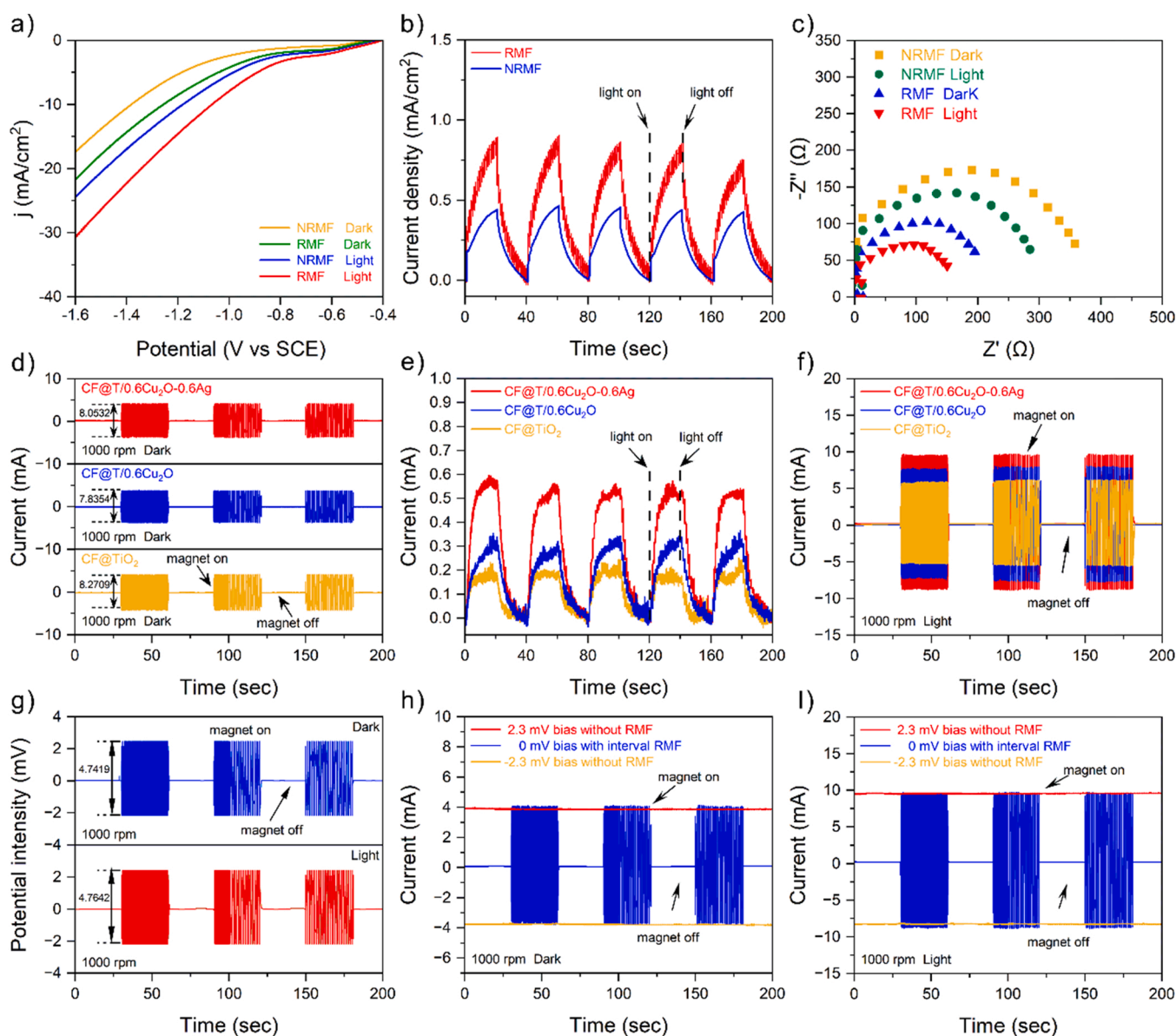


Fig. 5. (a) Liner sweep voltammograms (LSV) of CF@T/0.6Cu₂O-0.6Ag catalysts under different conditions, (b) Transient photocurrent response CF@T/0.6Cu₂O-0.6Ag catalysts under RMF and NRMF conditions, (c) EIS Nyquist plots of CF@T/0.6Cu₂O-0.6Ag catalysts under different conditions, (d) Induced current of different photocatalysts under 1000 rpm RMF without light irradiation, (e) Photocurrent of different catalysts, (f) Induced current of different photocatalysts under 1000 rpm RMF with light irradiation, (g) Open circuit potential of CF@T/0.6Cu₂O-0.6Ag catalysts with 1000 rpm RMF under different conditions, (h) Comparison of current with external ± 2.3 mV bias and rotating magnetic field induced current in dark condition, (i) Comparison of current with external ± 2.3 mV bias and rotating magnetic field induced current with light irradiation.

0.6Ag catalysts on the FTO glass, no matter there is a rotating magnetic field or not, the yield of products showed a little different and similar to that of CF@T/0.6Cu₂O-0.6Ag without magnetic field. The main difference between the FTO@T/0.6Cu₂O-0.6Ag and the CF@T/0.6Cu₂O-0.6Ag is the metallic conductor, the motional electromotive force generated by FTO glass cutting the magnetic induction lines is negligible. This indicates that the in-situ micro electric field derived from the motional electromotive force is crucial in improving photocatalytic activity. Fig S13 is the comparison of products between CF@TiO₂ and CF@T/0.6Cu₂O-0.6Ag under 1000 rpm RMF or not. The yield of CO by CF@TiO₂ catalysts gained from 1.24 to 2.07 $\mu\text{mol}\cdot\text{g}^{-1}$. When it comes to CF@T/0.6Cu₂O-0.6Ag, the production of CO expands to 71.66 $\mu\text{mol}\cdot\text{g}^{-1}$. This could be because the rotating magnetic field further enhances the charge separation and transportation in the Z-scheme system. The rotating magnetic field could also be helpful in improving the stability of the catalysts, we did not observe the apparent photocorrosion of CF@T/0.6Cu₂O-0.6Ag catalysts after multiple reactions (Fig S7b).

The photoelectrochemical testaments were also conducted under the RMF condition. The photocurrent density difference of CF@T/0.6Cu₂O-0.6Ag catalysts between 1000 rpm RMF Light and NRMF (Without Rotating Magnetic Field) Light is 6.4 mA/cm² for the same bias voltage (Fig. 5a). The transient photocurrent response of CF@T/0.6Cu₂O-0.6Ag in different conditions is shown in Fig. 5b. The maximum photocurrent density of the 1000 rpm RMF condition (0.89 mA/cm²) was almost twice that of the NRMF circumstance (0.44 mA/cm²). Notably, there is an amplitude current density (about 0.07 mA/cm²) after introducing RMF. The amplitude can be attributed to the motional electromotive force. The LSV and transient photocurrent response gave strong proof that the carrier density will increase under the RMF condition and thus contribute to CO₂ conversion. The EIS Nyquist plots of CF@T/0.6Cu₂O-0.6Ag catalysts were carried out under four different conditions: NRMF-Dark, NRMF-Light, 1000 rpm RMF-Dark, and 1000 rpm RMF-Light (Fig. 5c). Due to the photoconductive effect, the charge transfer resistances decreased slightly after light irradiation. When coupling RMF, the charge transfer resistances decreased apparently and had a smaller semicircle. Indicating that the charge transfer resistance of photocatalysts can be reduced by a magnetic field [82].

To further explore the coupling effect between the photo and magnetic field, we tested the induced current and open circuit potential through the electrochemical workstation which acted as a multimeter (Fig S14) [91]. Fig S15 shows the change of induced current of CF@T/0.6Cu₂O-0.6Ag catalysts under dark and light conditions. When the CF@T/0.6Cu₂O-0.6Ag catalysts did not cut the magnetic induction line, there are no current detected, with the increase of rotating speed, the peak current increased as well. Besides we tested the induced current of CF@TiO₂, CF@T/0.6Cu₂O, and CF@T/0.6Cu₂O-0.6Ag catalysts at 1000 rpm RMF in the dark and light conditions (Fig. 5d and Fig. 5f). The peak current in the dark condition is 4.14 mA, 3.93 mA, and 4.03 mA, respectively. While under light irradiation, different catalysts showed different responses, the intensity of the peak current in the order of CF@TiO₂ (5.78 mA), CF@T/0.6Cu₂O (7.77 mA), and CF@T/0.6Cu₂O-0.6Ag (9.59 mA). Notably, the peak current in the RMF dark condition is almost the same. This may be because the current all comes from the motional electromotive force generated by the CF substrate cutting the magnetic induction lines in the RMF. On the other hand, the current under RMF light conditions is much stronger than that under dark conditions. This increased photocurrent comes from the photo-induced charges. Fig. 5e depicts the photo-induced current of CF@TiO₂ (0.18 mA), CF@T/0.6Cu₂O (0.28 mA), and CF@T/0.6Cu₂O-0.6Ag (0.54 mA) without rotating magnetic field. Take CF@T/0.6Cu₂O-0.6Ag as an example. It is obviously that the peak current induced from the coupling of photo and rotating magnet field (9.59 mA, 1000 rpm Light) is better than the simple addition of peak current induced from light irradiation (0.54 mA, Light) and rotating magnet field (4.03 mA, 1000 rpm) individually. With the introduction of the rotating magnetic field under light irradiation condition, the

separation of the photogenerated charges is strengthened by the motional electromotive force and the photo-induced current is supposed to increase. The rotating magnetic field enhanced photo current and the induced current realize the strong current in Fig. 5f together. Furthermore, the photo-magnetic field coupling effect enhances the charge transfer process in catalysts that have efficient charge transfer pathway, thus CF@T/0.6Cu₂O-0.6Ag catalysts showed a better current response. Fig. 5g shows the open circuit potential of CF@T/0.6Cu₂O-0.6Ag catalysts at 1000 rpm RMF in dark and light conditions, the potential can be seen as the motional electromotive force in the CF substrate. The difference in peak-to-valley potential is 4.7 mV approximately which means the intensity of motional electromotive force in the CF substrate is 2.3 mV. So we tested the current in dark and light conditions with an external ± 2.3 mV bias and compared them with that of 1000 rpm RMF (Fig. 5h and Fig. 5i). Interestingly, the current generated by external bias is close to the peak current induced by RMF. This may indicate that the polarized charges generated from metallic conductors cutting magnetic induction lines act as an in situ electric field. Considering the above results, we can conclude that the separation and transportation of photogenerated carriers can be remarkably enhanced by the synergistic effect of the photo and magnetic field.

Inspired by the improvement of the photocatalytic CO₂ reduction for the CF@T/0.6Cu₂O-0.6Ag catalysts under RMF conditions and the results of the photoelectrochemical test above. We present the possible mechanism of Z-scheme CF@T/0.6Cu₂O-0.6Ag catalysts enhanced by the synergistic effect of the photo and magnetic field in photocatalytic CO₂ reduction. According to the right-hand rule, when the metallic conductor is cutting the magnetic induction lines. There will be Lorentz force inside the metal, thus the electrons inside the metal will be affected and polarize spontaneously according to the direction of Lorentz force (where the electric field direction points to the direction of positive charge accumulation). Fig. 6a shows four special positions, when the conductor is located in B and D positions in which the rotating direction is parallel to the magnetic induction line, there is no charge polarization. When the conductor is in A and C positions, where the rotating direction is vertical with the magnetic induction line, the motional electromotive force and the density of polarized charge in the CF substrate are the strongest.

The intensity and direction of the induced electromotive force change periodically like simple harmonic vibration. Focus on the A and C positions, a large number of charges accumulated on the surface of both ends of CF, one side is positive charge and the other is negative and the number of charges decreases from ends towards the center. On the side where negative charges gather, some of the photo-induced electrons on the CB of TiO₂ and Cu₂O will be repulsed and moved away from the CF side. While on the other side that accumulates positive charges, the photogenerated electrons will be attracted and move toward the CF side. It is just like loading a special electric field which drives the photo-generated carriers to move in opposite directions. The two conditions mentioned above both enhance the charge separation in TiO₂ and Cu₂O and allow electrons on the CB of TiO₂ to transfer and recombine with the holes on the VB of Cu₂O. So, the electron density on the CB of Cu₂O and Ag nanoparticles will increase to some extent and further participate in the CO₂ reduction reaction (Fig. 6b). The motional electromotive force generated by metallic substrate cutting magnetic induction lines caused the in situ spatial electric field, which improves the separation and transportation of electrons and holes of photocatalysts in the Z-scheme system, thus promoting a higher photocatalytic efficiency.

3. Conclusions

In summary, we constructed a monolithic Z-scheme CF@T/0.6Cu₂O-0.6Ag catalyst to improve the efficiency of converting CO₂ to CO and CH₄. The decoration of Cu₂O and Ag nanoparticles enhanced the chemisorption of CO₂ and the successful construction of the Z-scheme of TiO₂ and Cu₂O enabled more efficient charge separation. Both of the

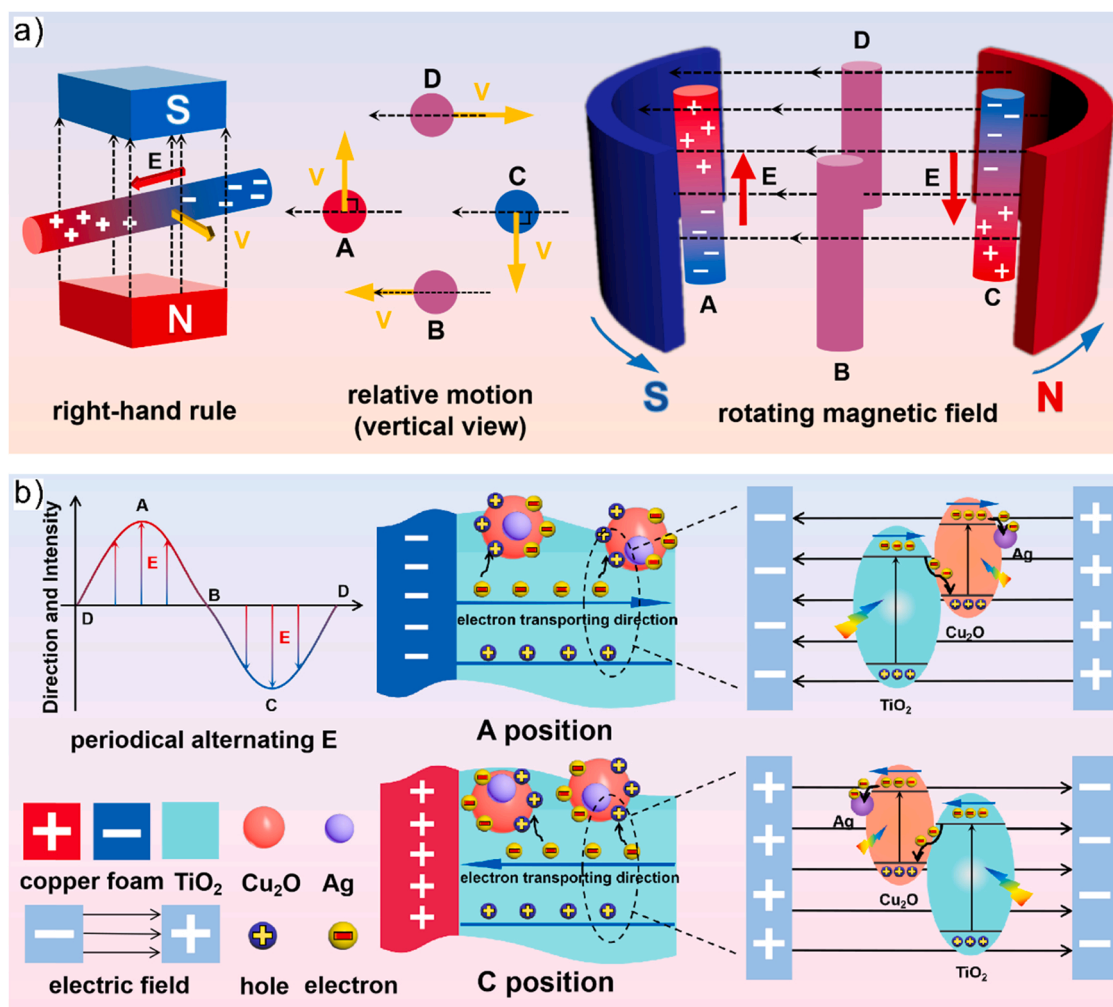


Fig. 6. (a-b) Diagram and proposed mechanism of enhanced Z-scheme CO₂ reduction process of CF@T/0.6Cu₂O-0.6Ag catalysts by solar-wind photocatalytic reactor.

above promote monolithic CF@T/0.6Cu₂O-0.6Ag catalyst a good photocatalytic efficiency compared with CF@TiO₂, improving the yield of CO from 1.24 $\mu\text{mol}\cdot\text{g}^{-1}\cdot\text{h}^{-1}$ to 25.58 $\mu\text{mol}\cdot\text{g}^{-1}\cdot\text{h}^{-1}$. Upon the coupling of photo and magnetic field through a solar-wind photocatalytic reactor, the productivity of CO and CH₄ increased sharply to 71.66 $\mu\text{mol}\cdot\text{g}^{-1}$ and 12.59 $\mu\text{mol}\cdot\text{g}^{-1}$ within one hour, which is almost three times than no magnetic field condition. The motional electromotive force generated by CF cutting magnetic induction lines in a rotating magnetic field results in the polarized charges in CF. The charge polarization enhances the separation and transportation of charge carriers in the Z-scheme system. With the influence of in situ space electric field generated from the polarized charges, the electrons in the CB of TiO₂ will recombine with the holes in the VB of Cu₂O and the electrons in the CB of Cu₂O will transport to Ag more than usual, giving opportunities for more carriers per unit of time to participate in the surface reaction. The coupling strategy of photo-magnetic in this paper provides a new idea for multi-field photocatalysis and makes useful exploration for practical application of solar-wind photocatalysis in the future.

CRediT authorship contribution statement

Biao Kong: Conceptualization, Methodology, Validation, Formal analysis, Investigation, Writing – original draft. **Yuqi Ren:** Formal analysis, Data curation, Visualization. **Maochang Liu:** Conceptualization, Writing – review & editing. **Jiancheng Zhou:** Validation, Supervision. **Ke Wang:** Investigation, Methodology, Formal analysis. **Nan**

Wang: Methodology, Validation. **Naixu Li:** Conceptualization, Writing – review & editing, Supervision, Project administration, Funding acquisition.

Declaration of Competing Interest

The authors declare that they have no known competing financial interests or personal relationships that could have appeared to influence the work reported in this paper.

Data Availability

Data will be made available on request.

Acknowledgments

This work was financially supported by the National Natural Science Foundation of China (No. 22078057), the National Natural Science Foundation of China (Key Program of joint fund No. U22A20435), the Fundamental Research Funds for the Central Universities (No. 2242023K5001), and the Scientific and Technological Innovation Project of Carbon Emission Peak and Carbon Neutrality of Jiangsu Province (No. BK20220001).

Appendix A. Supporting information

Supplementary data associated with this article can be found in the online version at [doi:10.1016/j.apcatb.2023.122858](https://doi.org/10.1016/j.apcatb.2023.122858).

References

- [1] J. Ran, M. Jaroniec, S.Z. Qiao, Cocatalysts in semiconductor-based photocatalytic CO₂ reduction: achievements, challenges, and opportunities, *Adv. Mater.* 30 (2018), 201704649, <https://doi.org/10.1002/adma.201704649>.
- [2] W. Gao, T. Zhou, Y. Gao, B. Louis, D. O'Hare, Q. Wang, Molten salts-modified MgO-based adsorbents for intermediate-temperature CO₂ capture: a review, *J. Energy Chem.* 26 (2017) 830–838, <https://doi.org/10.1016/j.jechem.2017.06.005>.
- [3] K. Li, B. Peng, T. Peng, Recent advances in heterogeneous photocatalytic CO₂ conversion to solar fuels, *ACS Catal.* 6 (2016) 7485–7527, <https://doi.org/10.1021/acscatal.6b02089>.
- [4] Y. Wang, H. Huang, Z. Zhang, C. Wang, Y. Yang, Q. Li, D. Xu, Lead-free perovskite Cs₂AgBiBr₆/g-C₃N₄ Z-scheme system for improving CH₄ production in photocatalytic CO₂ reduction, *Appl. Catal. B Environ.* 282 (2021), 119570, <https://doi.org/10.1016/j.apcatb.2020.119570>.
- [5] F. Yu, C. Wang, Y. Li, H. Ma, R. Wang, Y. Liu, N. Suzuki, C. Terashima, B. Ohtani, T. Ochiai, A. Fujishima, X. Zhang, Enhanced solar photothermal catalysis over solution plasma activated TiO₂, *Adv. Sci.* 7 (2020), 2000204, <https://doi.org/10.1002/advsc.202000204>.
- [6] G. Han, F. Xu, B. Cheng, Y. Li, J. Yu, L. Zhang, Enhanced photocatalytic H₂O₂ production over inverse opal ZnO/Polydopamine S-scheme heterojunctions, *Acta Phys. -Chim. Sin.* 38 (7) (2022), 2112037, <https://doi.org/10.3866/PKU.WHXB202112037>.
- [7] M. Wang, M. Shen, X. Jin, J. Tian, Y. Shao, L. Zhang, Y. Li, J. Shi, Exploring the enhancement effects of hetero-metal doping in CeO₂ on CO₂ photocatalytic reduction performance, *Chem. Eng. J.* 427 (2022), 130987, <https://doi.org/10.1016/j.cej.2021.130987>.
- [8] X. Wang, Z. Li, J. Shi, Y. Yu, One-dimensional titanium dioxide nanomaterials: nanowires, nanorods, and nanobelts, *Chem. Rev.* 114 (2014) 9346–9384, <https://doi.org/10.1021/cr400633s>.
- [9] Z. Xiong, Z. Lei, C.-C. Kuang, X. Chen, B. Gong, Y. Zhao, J. Zhang, C. Zheng, J.C. S. Wu, Selective photocatalytic reduction of CO₂ into CH₄ over Pt-Cu₂O TiO₂ nanocrystals: The interaction between Pt and Cu₂O cocatalysts, *Appl. Catal. B Environ.* 202 (2017) 695–703, <https://doi.org/10.1016/j.apcatb.2016.10.001>.
- [10] M. Hussain, P. Akhter, N. Russo, G. Saracco, New optimized mesoporous silica incorporated isolated Ti materials towards improved photocatalytic reduction of carbon dioxide to renewable fuels, *Chem. Eng. J.* 278 (2015) 279–292, <https://doi.org/10.1016/j.cej.2014.08.095>.
- [11] Z. Xiong, Z. Lei, Y. Li, L. Dong, Y. Zhao, J. Zhang, A review on modification of facet-engineered TiO₂ for photocatalytic CO₂ reduction, *J. Photochem. Photobiol. C* 36 (2018) 24–47, <https://doi.org/10.1016/j.jphotochemrev.2018.07.002>.
- [12] Y. Mao, P. Wang, S. Zhan, Shedding light on the role of interfacial chemical bond in heterojunction photocatalysis, *Nano Res.* 15 (2022) 10158–10170, <https://doi.org/10.1007/s12274-022-4593-y>.
- [13] H. Li, H. Gong, Z. Jin, In₂O₃-modified three-dimensional nanoflower MoS_x form S-scheme heterojunction for efficient hydrogen production, *Acta Phys. -Chim. Sin.* 38 (12) (2022), 2201037, <https://doi.org/10.3866/PKU.WHXB202201037>.
- [14] L. Zhou, Y. Li, Y. Zhang, L. Qiu, Y. Xing, A 0D/2D Bi₄V₂O₁₁/g-C₃N₄ S-scheme heterojunction with rapid interfacial charges migration for photocatalytic antibiotic degradation, *Acta Phys. -Chim. Sin.* 38 (7) (2022), 2112027, <https://doi.org/10.3866/PKU.WHXB202112027>.
- [15] Y. Tachibana, L. Vayssieres, J.R. Durrant, Artificial photosynthesis for solar water-splitting, *Nat. Photonics* 6 (2012) 511–518, <https://doi.org/10.1038/nphoton.2012.175>.
- [16] J. Yan, C. Wang, H. Ma, Y. Li, Y. Liu, N. Suzuki, C. Terashima, A. Fujishima, X. Zhang, Photothermal synergic enhancement of direct Z-scheme behavior of Bi₄TaO₈Cl/W₁₈O₄₉ heterostructure for CO₂ reduction, *Appl. Catal. B Environ.* 268 (2020), 118401, <https://doi.org/10.1016/j.apcatb.2019.118401>.
- [17] K. Qi, B. Cheng, J. Yu, W. Ho, A review on TiO₂-based Z-scheme photocatalysts, *Chin. J. Catal.* 38 (2017) 1936–1955, [https://doi.org/10.1016/s1872-2067\(17\)62962-0](https://doi.org/10.1016/s1872-2067(17)62962-0).
- [18] X. Hu, R.-H. Guo, X. Chen, Z.-X. Bi, J. Wang, W.-G. Pan, Bismuth-based Z-scheme structure for photocatalytic CO₂ reduction: a review, *J. Environ. Chem. Eng.* 10 (2022), 108582, <https://doi.org/10.1016/j.jecec.2022.108582>.
- [19] Q. Zhai, S. Xie, W. Fan, Q. Zhang, Y. Wang, W. Deng, Y. Wang, Photocatalytic conversion of carbon dioxide with water into methane: platinum and copper(I) oxide co-catalysts with a core-shell structure, *Angew. Chem. Int. Ed.* 52 (2013) 5776–5779, <https://doi.org/10.1002/anie.201301473>.
- [20] P. Yang, Z.J. Zhao, X. Chang, R. Mu, S. Zha, G. Zhang, J. Gong, The functionality of surface hydroxy groups on the selectivity and activity of carbon dioxide reduction over cuprous oxide in aqueous solutions, *Angew. Chem. Int. Ed.* 57 (2018) 7724–7728, <https://doi.org/10.1002/anie.201801463>.
- [21] B. Weng, M.-Y. Qi, C. Han, Z.-R. Tang, Y.-J. Xu, Photocorrosion inhibition of semiconductor-based photocatalysts: basic principle, current development, and future perspective, *ACS Catal.* 9 (2019) 4642–4687, <https://doi.org/10.1021/acscatal.9b00313>.
- [22] K. Iizuka, T. Wato, Y. Miseki, K. Saito, A. Kudo, Photocatalytic reduction of carbon dioxide over Ag cocatalyst-loaded Al_{0.4}Ti_{0.6}O₃ (A = Ca, Sr, and Ba) using water as a reducing reagent, *J. Am. Chem. Soc.* 133 (2011) 20863–20868, <https://doi.org/10.1021/ja207586e>.
- [23] L. Yuan, B. Weng, J.C. Colmenares, Y. Sun, Y.J. Xu, Multichannel charge transfer and mechanistic insight in metal decorated 2D–2D Bi₂WO₆-TiO₂ cascade with enhanced photocatalytic performance, *Small* 13 (2017), 1702253, <https://doi.org/10.1002/smll.201702253>.
- [24] W. Zhang, A.R. Mohamed, W.J. Ong, Z-scheme photocatalytic systems for carbon dioxide reduction: where are we now? *Angew. Chem. Int. Ed.* 59 (2020) 22894–22915, <https://doi.org/10.1002/anie.201914925>.
- [25] J. Xiao, X. Liu, L. Pan, C. Shi, X. Zhang, J.-J. Zou, Heterogeneous photocatalytic organic transformation reactions using conjugated polymers-based materials, *ACS Catal.* 10 (2020) 12256–12283, <https://doi.org/10.1021/acscatal.0c03480>.
- [26] J. Li, Q. Pei, R. Wang, Y. Zhou, Z. Zhang, Q. Cao, D. Wang, W. Mi, Y. Du, Enhanced photocatalytic performance through magnetic field boosting carrier transport, *ACS Nano* 12 (2018) 3351–3359, <https://doi.org/10.1021/acsnano.7b08770>.
- [27] C. Hu, S. Tu, N. Tian, T. Ma, Y. Zhang, H. Huang, Photocatalysis enhanced by external fields, *Angew. Chem. Int. Ed.* 60 (2021) 16309–16328, <https://doi.org/10.1002/anie.202009518>.
- [28] X. Li, W. Wang, F. Dong, Z. Zhang, L. Han, X. Luo, J. Huang, Z. Feng, Z. Chen, G. Jia, T. Zhang, Recent advances in noncontact external-field-assisted photocatalysis: from fundamentals to applications, *ACS Catal.* 11 (2021) 4739–4769, <https://doi.org/10.1021/acscatal.0c05354>.
- [29] L. Xiao, X. Xu, Y. Jia, G. Hu, J. Hu, B. Yuan, Y. Yu, G. Zou, Pyroelectric nanoplates for reduction of CO₂ to methanol driven by temperature-variation, *Nat. Commun.* 12 (2021) 318, <https://doi.org/10.1038/s41467-020-20517-1>.
- [30] S. Tiewcharoen, C. Warakulwit, V. Lapeyre, P. Garrigue, L. Fourier, C. Elissalde, S. Buffiere, P. Legros, M. Gayot, J. Limtrakul, A. Kuhn, Anisotropic metal deposition on TiO₂ particles by electric-field-induced charge separation, *Angew. Chem. Int. Ed.* 56 (2017) 11431–11435, <https://doi.org/10.1002/anie.201704393>.
- [31] B. Hu, L. Yan, M. Shao, Magnetic-field effects in organic semiconducting materials and devices, *Adv. Mater.* 21 (2009) 1500–1516, <https://doi.org/10.1002/adma.200802386>.
- [32] Y. Zhao, Z. Huang, W. Chang, C. Wei, X. Feng, L. Ma, X. Qi, Z. Li, Microwave-assisted solvothermal synthesis of hierarchical TiO₂ microspheres for efficient electro-field-assisted-photocatalytic removal of tributyltin in tannery wastewater, *Chemosphere* 179 (2017) 75–83, <https://doi.org/10.1016/j.chemosphere.2017.03.084>.
- [33] W. Gao, R. Peng, Y. Yang, X. Zhao, C. Cui, X. Su, W. Qin, Y. Dai, Y. Ma, H. Liu, Y. Sang, Electron spin polarization-enhanced photoinduced charge separation in ferromagnetic ZnFe₂O₄, *ACS Energy Lett.* 6 (2021) 2129–2137, <https://doi.org/10.1021/acsenenergylett.1c00682>.
- [34] L. Pan, M. Ai, C. Huang, L. Yin, X. Liu, R. Zhang, S. Wang, Z. Jiang, X. Zhang, J. J. Zou, W. Mi, Manipulating spin polarization of titanium dioxide for efficient photocatalysis, *Nat. Commun.* 11 (2020) 418, <https://doi.org/10.1038/s41467-020-14333-w>.
- [35] X. Zhao, W. Gao, Q. Liu, C. Cui, W. Zhou, X. Wang, X.L. Zhang, L. Zhao, Y. Sang, H. Liu, Enhanced photo-induced carrier separation of CdS/moS₂ via micro-potential of Mo microsheet derived from electromagnetic induction, *Chem. Eng. J.* 404 (2021), 126972, <https://doi.org/10.1016/j.cej.2020.126972>.
- [36] M. Wakasa, S. Suda, H. Hayashi, N. Ishii, M. Okano, Magnetic field effect on the photocatalytic reaction with ultrafine TiO₂, Part., *J. Phys. Chem. B* 108 (2004) 11882–11885, <https://doi.org/10.1021/jp037232f>.
- [37] W. Gao, J. Lu, S. Zhang, X. Zhang, Z. Wang, W. Qin, J. Wang, W. Zhou, H. Liu, Y. Sang, Suppressing photoinduced charge recombination via the Lorentz force in a photocatalytic system, *Adv. Sci.* 6 (2019), 1901244, <https://doi.org/10.1002/advsc.201901244>.
- [38] W. Gao, Q. Liu, S. Zhang, Y. Yang, X. Zhang, H. Zhao, W. Qin, W. Zhou, X. Wang, H. Liu, Y. Sang, Electromagnetic induction derived micro-electric potential in metal-semiconductor core-shell hybrid nanostructure enhancing charge separation for high performance photocatalysis, *Nano Energy* 71 (2020), 104624, <https://doi.org/10.1016/j.nanoen.2020.104624>.
- [39] G. Liu, S. Zhang, X. Wu, R. Lin, Fabrication of rutile TiO₂ nanorod arrays on a copper substrate for high-performance lithium-ion batteries, *RSC Adv.* 6 (2016) 55671–55675, <https://doi.org/10.1039/c6ra10285a>.
- [40] E. Hosono, S. Fujihara, K. Kakiuchi, H. Imai, Growth of submicrometer-scale rectangular parallelepiped rutile TiO₂ films in aqueous TiCl₃ solutions under hydrothermal conditions, *J. Am. Chem. Soc.* 126 (2004) 7790–7791, <https://doi.org/10.1021/ja048820p>.
- [41] F. Zhang, Y.-H. Li, M.-Y. Qi, Z.-R. Tang, Y.-J. Xu, Boosting the activity and stability of Ag-Cu₂O/ZnO nanorods for photocatalytic CO₂ reduction, *Appl. Catal. B Environ.* 268 (2020), 118380, <https://doi.org/10.1016/j.apcatb.2019.118380>.
- [42] J.C. Wang, L. Zhang, W.X. Fang, J. Ren, Y.Y. Li, H.C. Yao, J.S. Wang, Z.J. Li, Enhanced photoreduction CO₂ activity over direct Z-scheme alpha-Fe₂O₃/Cu₂O heterostructures under visible light irradiation, *ACS Appl. Mater. Interfaces* 7 (2015) 8631–8639, <https://doi.org/10.1021/acsaami.5b00822>.
- [43] J. Liu, Z. Gao, H. Han, D. Wu, F. Xu, H. Wang, K. Jiang, Mesoporous Cu₂O submicro-spheres, facile synthesis and the selective adsorption properties, *Chem. Eng. J.* 185–186 (2012) 151–159, <https://doi.org/10.1016/j.cej.2012.01.064>.
- [44] H. Jung, S.Y. Lee, C.W. Lee, M.K. Cho, D.H. Won, C. Kim, H.S. Oh, B.K. Min, Y. J. Hwang, Electrochemical fragmentation of Cu₂O nanoparticles enhancing selective C-C coupling from CO₂ reduction reaction, *J. Am. Chem. Soc.* 141 (2019) 4624–4633, <https://doi.org/10.1021/jacs.8b11237>.
- [45] X. Cheng, P. Dong, Z. Huang, Y. Zhang, Y. Chen, X. Nie, X. Zhang, Green synthesis of plasmonic Ag nanoparticles anchored TiO₂ nanorod arrays using cold plasma for visible-light-driven photocatalytic reduction of CO₂, *J. CO₂ Util.* 20 (2017) 200–207, <https://doi.org/10.1016/j.jcou.2017.04.009>.

- [46] K. Wada, C.S.K. Ranasinghe, R. Kuriki, A. Yamakata, O. Ishitani, K. Maeda, Interfacial manipulation by rutile TiO₂ nanoparticles to boost CO₂ Reduction into CO on a metal-complex/semiconductor hybrid photocatalyst, *ACS Appl. Mater. Interfaces* 9 (2017) 23869–23877, <https://doi.org/10.1021/acsami.7b07484>.
- [47] M. Zhang, X. Xuan, W. Wang, C. Ma, Z. Lin, Anode photovoltage compensation-enabled synergistic CO₂ photoelectrocatalytic reduction on a flower-like graphene-decorated Cu foam cathode, *Adv. Funct. Mater.* 30 (2020), <https://doi.org/10.1002/adfm.202005983>.
- [48] V.R. Djokic, A.D. Marinkovic, R.D. Petrovic, O. Ersen, S. Zafeirotos, M. Mitric, C. Ophus, V.R. Radmilovic, D.T. Janackovic, Highly active rutile TiO₂ nanocrystalline photocatalysts, *ACS Appl. Mater. Interfaces* 12 (2020) 33058–33068, <https://doi.org/10.1021/acsami.0c03150>.
- [49] F. Xu, J. Zhang, B. Zhu, J. Yu, J. Xu, CuInS₂ sensitized TiO₂ hybrid nanofibers for improved photocatalytic CO₂ reduction, *Appl. Catal. B Environ.* 230 (2018) 194–202, <https://doi.org/10.1016/j.apcatb.2018.02.042>.
- [50] Q. Zhang, H. Zhang, B. Gu, Q. Tang, Q. Cao, W. Fang, Sunlight-driven photocatalytic oxidation of 5-hydroxymethylfurfural over a cuprous oxide-anatase heterostructure in aqueous phase, *Appl. Catal. B Environ.* 320 (2023), 122006, <https://doi.org/10.1016/j.apcatb.2022.122006>.
- [51] X. Qiu, M. Miyauchi, K. Sunada, M. Minoshima, M. Liu, Y. Lu, D. Li, Y. Shimodaira, Y. Hosogi, Y. Kuroda, Hybrid Cu₂O/TiO₂ nanocomposites as risk-reduction materials in indoor environments, *ACS Nano* 2 (2012) 1609–1618, <https://doi.org/10.1021/nn2045888>.
- [52] B. Liu, J. Wang, J. Yang, X. Zhao, Charge carrier interfacial transfer pathways from TiO₂ and Au/TiO₂ nanorod arrays to electrolyte and the association with photocatalysis, *Appl. Surf. Sci.* 464 (2019) 367–375, <https://doi.org/10.1016/j.apsusc.2018.09.031>.
- [53] N. Li, B. Wang, Y. Si, F. Xue, J. Zhou, Y. Lu, M. Liu, Toward high-value hydrocarbon generation by photocatalytic reduction of CO₂ in water vapor, *ACS Catal.* 9 (2019) 5590–5602, <https://doi.org/10.1021/acscatal.9b00223>.
- [54] Y. Lu, X. Zhang, Y. Chu, H. Yu, M. Huo, J. Qu, J.C. Crittenden, H. Huo, X. Yuan, Cu₂O nanocrystals/TiO₂ microspheres film on a rotating disk containing long-afterglow phosphor for enhanced round-the-clock photocatalysis, *Appl. Catal. B Environ.* 224 (2018) 239–248, <https://doi.org/10.1016/j.apcatb.2017.10.054>.
- [55] Q. Wei, Y. Wang, H. Qin, J. Wu, Y. Lu, H. Chi, F. Yang, B. Zhou, H. Yu, J. Liu, Construction of rGO wrapping octahedral Ag-Cu₂O heterostructure for enhanced visible light photocatalytic activity, *Appl. Catal. B Environ.* 227 (2018) 132–144, <https://doi.org/10.1016/j.apcatb.2018.01.003>.
- [56] L. Yu, G. Li, X. Zhang, X. Ba, G. Shi, Y. Li, P.K. Wong, J.C. Yu, Y. Yu, Enhanced activity and stability of carbon-decorated cuprous oxide mesoporous nanorods for CO₂ reduction in artificial photosynthesis, *ACS Catal.* 6 (2016) 6444–6454, <https://doi.org/10.1021/acscatal.6b01455>.
- [57] X. Wang, Z. Jiang, H. Chen, K. Wang, X. Wang, Photocatalytic CO₂ reduction with water vapor to CO and CH₄ in a recirculation reactor by Ag-Cu₂O/TiO₂ Z-scheme heterostructures, *J. Alloy. Compd.* 896 (2022), 163030, <https://doi.org/10.1016/j.jallcom.2021.163030>.
- [58] J. Zhou, F. Pan, Q. Yao, Y. Zhu, H. Ma, J. Niu, J. Xie, Achieving efficient and stable electrochemical nitrate removal by in-situ reconstruction of Cu₂O/Cu electroactive nanocatalysts on Cu foam, *Appl. Catal. B Environ.* 317 (2022), 121811, <https://doi.org/10.1016/j.apcatb.2022.121811>.
- [59] X. Wen, X. Chang, A. Li, X. Yang, F. Tian, Z. Liu, N. Copner, P. Teng, L. Yuan, ZnO/Cu₂O heterojunction integrated fiber-optic biosensor for remote detection of cysteine, *Biosens. Bioelectron.* 223 (2023), 115021, <https://doi.org/10.1016/j.bios.2022.115021>.
- [60] X. Li, S. Raza, C. Liu, Directly electrospinning synthesized Z-scheme heterojunction TiO₂@Ag/Cu₂O nanofibers with enhanced photocatalytic degradation activity under solar light irradiation, *J. Environ. Chem. Eng.* 9 (2021), 106133, <https://doi.org/10.1016/j.jece.2021.106133>.
- [61] J. Hou, J. Zhou, Y. Liu, Y. Yang, S. Zheng, Q. Wang, Constructing Ag₂O nanoparticle modified TiO₂ nanotube arrays for enhanced photocatalytic performances, *J. Alloy. Compd.* 849 (2020), 156493, <https://doi.org/10.1016/j.jallcom.2020.156493>.
- [62] F. Wei, L. Liu, C. Wang, X. Wu, Y. Du, Cu(Mn)MgAl mixed oxides with enhanced performance for simultaneous removal of NO_x and toluene: Insight into the better collaboration of CuO and MnO_x via layered double hydroxides (LDHs) precursor template, *Chem. Eng. J.* 462 (2023), 142150, <https://doi.org/10.1016/j.cej.2023.142150>.
- [63] S. Zhu, W. Liao, M. Zhang, S. Liang, Design of spatially separated Au and CoO dual cocatalysts on hollow TiO₂ for enhanced photocatalytic activity towards the reduction of CO₂ to CH₄, *Chem. Eng. J.* 361 (2019) 461–469, <https://doi.org/10.1016/j.cej.2018.12.095>.
- [64] D. Praveen Kumar, N. Lakshmana Reddy, B. Srinivas, V. Durgakumari, V. Roddatis, O. Bondarchuk, M. Karthik, Y. Ikuma, M.V. Shankar, Stable and active Cu_xO/TiO₂ nanostructured catalyst for proficient hydrogen production under solar light irradiation, *Sol. Energy Mater. Sol. Cells* 146 (2016) 63–71, <https://doi.org/10.1016/j.solmat.2015.11.030>.
- [65] J. Yu, J. Ran, Facile preparation and enhanced photocatalytic H₂-production activity of Cu(OH)₂ cluster modified TiO₂, *Energy Environ. Sci.* 4 (2011) 1364–1371, <https://doi.org/10.1039/c0ee00729c>.
- [66] W. Yuan, J. Yuan, J. Xie, C.M. Li, Polymer-mediated self-assembly of TiO₂@Cu₂O core-shell nanowire array for highly efficient photoelectrochemical water oxidation, *ACS Appl. Mater. Interfaces* 8 (2016) 6082–6092, <https://doi.org/10.1021/acsami.6b00030>.
- [67] S.V. Mohite, S. Kim, C. Lee, J. Bae, Y. Kim, Z-scheme heterojunction photocatalyst: Deep eutectic solvents-assisted synthesis of Cu₂O nanocluster improved hydrogen production of TiO₂, *J. Alloy. Compd.* 928 (2022), 167168, <https://doi.org/10.1016/j.jallcom.2022.167168>.
- [68] O. Ola, M.M. Maroto-Valer, Review of material design and reactor engineering on TiO₂ photocatalysis for CO₂ reduction, *J. Photochem. Photobiol. C* 24 (2015) 16–42, <https://doi.org/10.1016/j.jphotochemrev.2015.06.001>.
- [69] M. Yin, C. Wu, Y. Lou, C. Burda, J. Koberstein, Y. Zhu, S. O'Brien, Copper oxide nanocrystals, *J. Am. Chem. Soc.* 127 (2005) 9506–9511, <https://doi.org/10.1021/ja050006u>.
- [70] X. Li, B. Kang, F. Dong, Z. Zhang, X. Luo, L. Han, J. Huang, Z. Feng, Z. Chen, J. Xu, B. Peng, Z.L. Wang, Enhanced photocatalytic degradation and H₂/H₂O₂ production performance of S-pCN/WO_{2.72} S-scheme heterojunction with appropriate surface oxygen vacancies, *Nano Energy* 81 (2021), 105671, <https://doi.org/10.1016/j.nanoen.2020.105671>.
- [71] Y. Wu, Y. Li, H. Li, H. Guo, Q. Yang, X. Li, Tuning heterostructures interface of Cu₂O@HKUST-1 for enhanced photocatalytic degradation of tetracycline hydrochloride, *Sep. Purif. Technol.* 303 (2022), 122106, <https://doi.org/10.1016/j.seppur.2022.122106>.
- [72] M.E. Aguirre, R. Zhou, A.J. Eugene, M.I. Guzman, M.A. Grela, Cu₂O/TiO₂ heterostructures for CO₂ reduction through a direct Z-scheme: Protecting Cu₂O from photocorrosion, *Appl. Catal. B Environ.* 217 (2017) 485–493, <https://doi.org/10.1016/j.apcatb.2017.05.058>.
- [73] G. Liu, G. Hou, X. Mao, X. Qi, Y. Song, X. Ma, J. Wu, G. Luo, H. Yao, Q. Liu, Rational design of CeO₂/Bi₂O₃ flower-like nanosphere with Z-scheme heterojunction and oxygen vacancy for enhancing photocatalytic activity, *Chem. Eng. J.* 431 (2022), 133254, <https://doi.org/10.1016/j.cej.2021.133254>.
- [74] Q. Han, L. Li, W. Gao, Y. Shen, L. Wang, Y. Zhang, X. Wang, Q. Shen, Y. Xiong, Y. Zhou, Z. Zou, Elegant construction of ZnIn₂S₄/BiVO₄ hierarchical heterostructures as direct Z-scheme photocatalysts for efficient CO₂ photoreduction, *ACS Appl. Mater. Interfaces* 13 (2021) 15092–15100, <https://doi.org/10.1021/acsami.0c21266>.
- [75] H. Guo, S. Wan, Y. Wang, W. Ma, Q. Zhong, J. Ding, Enhanced photocatalytic CO₂ reduction over direct Z-scheme NiTiO₃/g-C₃N₄ nanocomposite promoted by efficient interfacial charge transfer, *Chem. Eng. J.* 412 (2021), 128646, <https://doi.org/10.1016/j.cej.2021.128646>.
- [76] F. Ye, Y. Su, X. Quan, S. Chen, H. Yu, H. Li, Constructing desired interfacial energy band alignment of Z-scheme TiO₂-Pd-Cu₂O hybrid by controlling the contact facet for improved photocatalytic performance, *Appl. Catal. B Environ.* 244 (2019) 347–355, <https://doi.org/10.1016/j.apcatb.2018.10.066>.
- [77] Z. Wang, L. Huang, B. Su, J. Xu, Z. Ding, S. Wang, Unravelling the promotional effect of La₂O₃ in Pt/La-TiO₂ catalysts for CO₂ hydrogenation, *Chemistry* 26 (2020) 517–523, <https://doi.org/10.1002/chem.201903946>.
- [78] N. Li, X. Zou, M. Liu, L. Wei, Q. Shen, R. Bibi, C. Xu, Q. Ma, J. Zhou, Enhanced visible light photocatalytic hydrogenation of CO₂ into methane over a Pd/Ce-TiO₂ nanocomposition, *J. Phys. Chem. C* 121 (2017) 25795–25804, <https://doi.org/10.1021/acs.jpcc.7b07298>.
- [79] Y. Pu, Y. Luo, X. Wei, J. Sun, L. Li, W. Zou, L. Dong, Synergistic effects of Cu₂O-decorated CeO₂ on photocatalytic CO₂ reduction: surface lewis acid/base and oxygen defect, *Appl. Catal. B Environ.* 254 (2019) 580–586, <https://doi.org/10.1016/j.apcatb.2019.04.093>.
- [80] S. Chen, T. Cao, Y. Gao, D. Li, F. Xiong, W. Huang, Probing surface structures of CeO₂, TiO₂, and Cu₂O nanocrystals with CO and CO₂ chemisorption, *J. Phys. Chem. C* 120 (2016) 21472–21485, <https://doi.org/10.1021/acs.jpcc.6b06158>.
- [81] S. Wei, Q. Heng, Y. Wu, W. Chen, X. Li, W. Shangguan, Improved photocatalytic CO₂ conversion efficiency on Ag loaded porous Ta₂O₅, *Appl. Surf. Sci.* 563 (2021), 150273, <https://doi.org/10.1016/j.apsusc.2021.150273>.
- [82] Z. Tang, F. Zhu, J. Zhou, W. Chen, K. Wang, M. Liu, N. Wang, N. Li, Monolithic NF@ZnO/Au@ZIF-8 photocatalyst with strong photo-thermal-magnetic coupling and selective-breathing effects for boosted conversion of CO₂ to CH₄, *Appl. Catal. B Environ.* 309 (2022), 121267, <https://doi.org/10.1016/j.apcatb.2022.121267>.
- [83] Y. Huang, K. Li, J. Zhou, J. Guan, F. Zhu, K. Wang, M. Liu, W. Chen, N. Li, Nitrogen-stabilized oxygen vacancies in TiO₂ for site-selective loading of Pt and CoO_x cocatalysts toward enhanced photoreduction of CO₂ to CH₄, *Chem. Eng. J.* 439 (2022), 135744, <https://doi.org/10.1016/j.cej.2022.135744>.
- [84] Y. Gao, Z. Tan, R. Yang, G. Huang, J. Bi, Integrating polyarylether-COFs with TiO₂ nanofibers for enhanced visible-light-driven CO₂ reduction in artificial photosynthesis, *Appl. Surf. Sci.* 605 (2022), 154605, <https://doi.org/10.1016/j.apsusc.2022.154605>.
- [85] Y. Yu, X. Dong, P. Chen, Q. Geng, H. Wang, J. Li, Y. Zhou, F. Dong, Synergistic effect of Cu single atoms and Au-Cu alloy nanoparticles on TiO₂ for efficient CO₂ photoreduction, *ACS Nano* 15 (2021) 14453–14464, <https://doi.org/10.1021/acsnano.1c03961>.
- [86] L. Wang, H. Tan, L. Zhang, B. Cheng, J. Yu, In-situ growth of few-layer graphene on ZnO with intimate interfacial contact for enhanced photocatalytic CO₂ reduction activity, *Chem. Eng. J.* 411 (2021), 128501, <https://doi.org/10.1016/j.cej.2021.128501>.
- [87] X. Li, W. He, C. Li, B. Song, S. Liu, Synergetic surface modulation of ZnO/Pt@ZIF-8 hybrid nanorods for enhanced photocatalytic CO₂ valorization, *Appl. Catal. B Environ.* 287 (2021), 119934, <https://doi.org/10.1016/j.apcatb.2021.119934>.
- [88] L. Liu, H. Zhao, J.M. Andino, Y. Li, Photocatalytic CO₂ reduction with H₂O on TiO₂ nanocrystals: comparison of anatase, rutile, and brookite polymorphs and exploration of surface chemistry, *ACS Catal.* 2 (2012) 1817–1828, <https://doi.org/10.1021/cs300273q>.
- [89] Y. Liu, B.-W. Tang, B. Wen, X.-B. Li, D.-F. Zou, Y.-F. Chai, Y. Xu, X.-L. Wei, W.-J. Yin, Non-metal atom modified SnS₂ sheet for CO₂ photoreduction with

- significant activity and selectivity improvements: a first-principles study, Appl. Surf. Sci. 584 (2022), 152618, <https://doi.org/10.1016/j.apsusc.2022.152618>.
- [90] H. Goto, H. Masegi, S.B. Sadale, K. Noda, Intricate behaviors of gas phase CO₂ photoreduction in high vacuum using Cu₂O-loaded TiO₂ nanotube arrays, J. CO₂ Util. 59 (2022), 101964, <https://doi.org/10.1016/j.jcou.2022.101964>.
- [91] J.L. Wang, H.J. Jiang, Z. He, J.W. Liu, R. Wang, W.R. Huang, L.T. Feng, X.F. Ren, Z. H. Hou, S.H. Yu, Radial nanowire assemblies under rotating magnetic field enabled efficient charge separation, Nano Lett. 20 (2020) 2763–2769, <https://doi.org/10.1021/acs.nanolett.0c00408>.